

Communication

Hot electron transistor with van der Waals base-collector heterojunction and high performance GaN emitter

Ahmad Zubair, Amirhasan Nourbakhsh, Jing Yong Hong, Meng Qi, Yi Song, Debdeep Jena, Jing Kong, Mildred S. Dresselhaus, and Tomas Palacios

Nano Lett., **Just Accepted Manuscript** • DOI: 10.1021/acs.nanolett.7b00451 • Publication Date (Web): 17 Apr 2017Downloaded from <http://pubs.acs.org> on April 17, 2017**Just Accepted**

“Just Accepted” manuscripts have been peer-reviewed and accepted for publication. They are posted online prior to technical editing, formatting for publication and author proofing. The American Chemical Society provides “Just Accepted” as a free service to the research community to expedite the dissemination of scientific material as soon as possible after acceptance. “Just Accepted” manuscripts appear in full in PDF format accompanied by an HTML abstract. “Just Accepted” manuscripts have been fully peer reviewed, but should not be considered the official version of record. They are accessible to all readers and citable by the Digital Object Identifier (DOI®). “Just Accepted” is an optional service offered to authors. Therefore, the “Just Accepted” Web site may not include all articles that will be published in the journal. After a manuscript is technically edited and formatted, it will be removed from the “Just Accepted” Web site and published as an ASAP article. Note that technical editing may introduce minor changes to the manuscript text and/or graphics which could affect content, and all legal disclaimers and ethical guidelines that apply to the journal pertain. ACS cannot be held responsible for errors or consequences arising from the use of information contained in these “Just Accepted” manuscripts.



Hot electron transistor with van der Waals base-collector heterojunction and high performance GaN emitter

Ahmad Zubair^{1}, Amirhasan Nourbakhsh¹, Jin-Yong Hong¹, Meng Qi², Yi Song¹, Debdeep Jena³, Jing Kong¹, Mildred Dresselhaus^{1,4}, Tomás Palacios¹*

¹Department of Electrical Engineering Computer Science, Massachusetts Institute of Technology, 77 Massachusetts Avenue, Cambridge, Massachusetts 02139, United States

²Electrical Engineering Department, University of Notre Dame, Notre Dame, Indiana 46556, United States

³School of Electrical and Computer Engineering, Cornell University, Ithaca, New York 14850, United States

⁴Department of Physics, Massachusetts Institute of Technology, 77 Massachusetts Avenue, Cambridge, Massachusetts 02139, United States

KEYWORDS Hot Electron transistor, Graphene, GaN, WSe₂, van der Waals heterostructure, Tunneling, Transition metal dichalcogenides

ABSTRACT

Single layer graphene is an ideal material for the base layer of hot electron transistors (HETs) for potential THz applications. The ultra-thin body and exceptionally long mean free path maximizes the probability for ballistic transport across the base of the HET. We demonstrate, for

1
2
3 the first time, the operation of a high performance HET using a graphene/WSe₂ van der Waals
4 (vdW) heterostructure as a base-collector barrier. The resulting device, with a GaN/AlN
5 heterojunction as emitter, exhibits a current density of 50 A/cm², DC current gain above 3 and
6 75% injection efficiency, which are record values among graphene-base HETs. These results not
7 only provide a scheme to overcome the limitations of graphene-base HETs toward THz
8 operation but are also the first demonstration of a GaN/vdW heterostructure in HETs, revealing
9 the potential for novel electronic and optoelectronic applications.
10
11
12
13
14
15
16
17
18
19
20
21
22
23
24
25
26

27 The hot electron transistor¹ is a promising device concept that could be used to overcome the
28 limitations of heterojunction bipolar transistors (HBTs) and high electron mobility transistors
29 (HEMTs) in ultra-high frequency applications. The HET is a unipolar and majority carrier device
30 where the base-to-emitter voltage controls the transport of ballistic hot electrons through a transit
31 layer smaller than the mean free path (λ_{mfp}) of the carriers. Hence, HETs have the potential to
32 exhibit a superior high frequency performance relative to HBTs (limited by the diffusion of the
33 minority carriers across the base) and HEMTs (limited by the saturation velocity of carriers and
34 the lithography of the gate)¹. As shown schematically in Figure 1a, a typical HET structure
35 consists of a hot electron injector (emitter/emitter-barrier stack), a transport layer (base) and a
36 hot electron analyzer or filter (collector-barrier/collector-stack). The HET can be considered as a
37 combination of two back-to-back diodes connected in series, namely the E-B diode and the B-C
38 diode. Under the operating conditions, the emitter-base (E-B) diode is forward biased ($V_{\text{BE}} > 0$
39 V) and electrons are injected into the base with an excess energy above the Fermi energy of the
40
41
42
43
44
45
46
47
48
49
50
51
52
53
54
55
56
57
58
59
60

1
2
3 base ($eV_{BE}-E_f$). If the base-collector (B-C) diode is then reverse biased ($V_{CB} > 0$ V), it will allow
4
5 the hot electrons reaching the base to travel to the collector with minimal scattering (quasi-
6
7 ballistically) (Figure 1a). However, if $V_{CB} < 0$ V, the energy barrier for the base electrons (shown
8
9 by the dotted lines in Figure 1a) will increase and majority of the injected electrons will
10
11 thermalize in the base by scattering and quantum mechanical reflection, and eventually
12
13 contribute to the base leakage current. Several material systems have been used for HET
14
15 development including metal thin films^{1, 2}, non-polar III-V semiconductor heterostructures³⁻⁶,
16
17 complex oxides⁷, and superconducting materials⁸. However, the successful demonstration of
18
19 high performance HETs have been limited by the technological inability to scale the base
20
21 thickness below the λ_{mfp} of the carriers and electrostatic decoupling of the collector from emitter.
22
23 In the thick base regions used so far, the injected hot electrons are thermalized in the base as a
24
25 result of inelastic (intra- and inter-valley⁶ electron–electron, electron–phonon) and elastic
26
27 (impurities) scattering. To reduce inter-valley scattering, wide bandgap materials such as GaN
28
29 have been recently used^{9, 10}, as they show large inter-valley separation. These GaN-based devices
30
31 have demonstrated excellent current gain (>10)¹¹ and current density ($\sim kA/cm^2$)^{11, 12} at room
32
33 temperature, however, similar to other bulk three-dimensional semiconductors, the growth of an
34
35 ultra-scaled base layer still remains a challenge.
36
37
38
39
40
41
42
43

44 Single atomic layer two-dimensional (2D) materials are naturally suitable for applications
45
46 requiring ultra-thin, defect-free films. Several vertical tunneling devices¹³ for both logic
47
48 (tunneling transistors¹⁴, barristors¹⁵) and high frequency applications (resonant tunneling
49
50 device¹⁶) have been demonstrated using these materials. Monolayer graphene, with ultra-high
51
52 mobility and a dangling-bond-free inert surface, is an ideal candidate as a low resistance,
53
54 scattering-free base material in HETs that can overcome the growth-related limitations in bulk
55
56
57
58
59
60

semiconductors. Theoretical studies have predicted that with an optimized structure, a maximum unity gain operating frequency (f_T) up to several THz¹⁷⁻²¹, I_{on}/I_{off} over 10^5 and high current gain^{19, 22, 23} can be achieved in graphene-base HETs (GHET). The initial experimental demonstrators of GHETs²⁴⁻²⁷ showed successful operation in terms of current modulation (on-off ratio $>10^5$) but suffered from low output current density ($\sim\mu\text{A}/\text{cm}^2$), low current gain, low injection efficiency, low output impedance and high threshold voltage. These limitations are not intrinsic to the use of graphene as a base material and can be overcome by a careful design and optimization of the device, which are the goals of the present work.

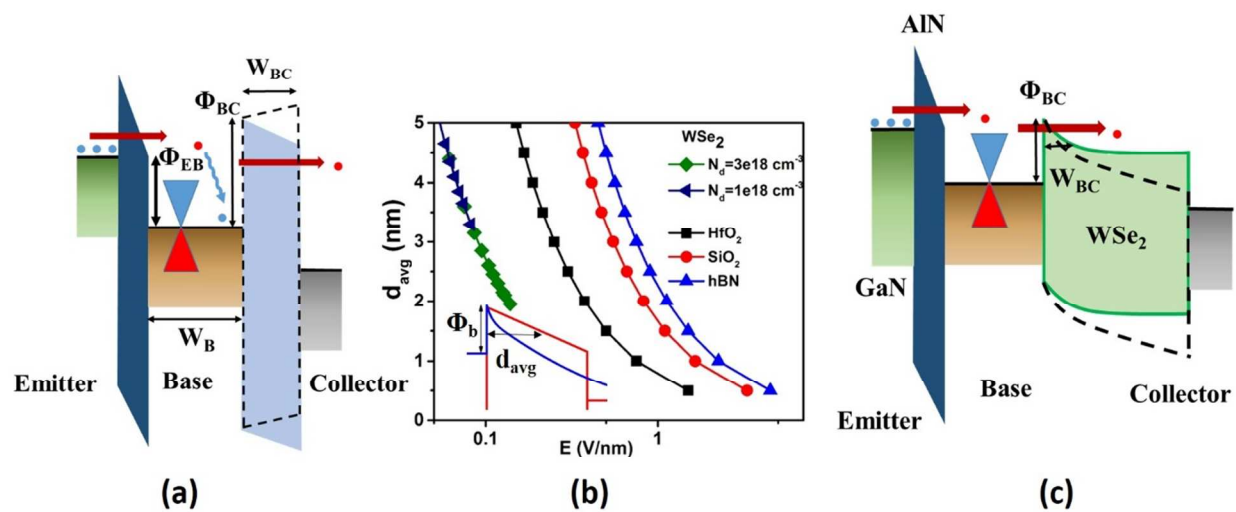


Figure 1. (a) Schematic energy band diagram of a GHET with an insulator-collector barrier along the vertical direction in the on-state for $V_{CB} > 0\text{V}$ (solid line) and $V_{CB} < 0\text{V}$ (dotted line), showing the carrier flow direction and relevant design parameters. (b) Average base-collector tunneling barrier width for electrons injected in graphene from the emitter as a function of electric field for different base-collector barrier materials. (c) Energy band diagram of the proposed GHET with a graphene/semiconductor Schottky barrier in the on-state for $V_{CB} > 0\text{V}$ (dotted line) and $V_{CB} < 0\text{V}$ (solid line).

1
2
3
4
5
6
7 One of the major shortcomings of the GHETs reported so far is the low output current density,
8
9 which can be increased by improving the i) emitter current (I_E) and ii) injection efficiency or
10
11 base transport factor, defined by:
12

$$\alpha = \frac{I_C}{I_E},$$

13
14
15
16
17
18
19
20 as shown in the band diagram in Figure 1a, the quantity I_E is dominated by the quantum
21
22 mechanical tunneling of electrons from the emitter to the base. According to the WKB
23
24 approximation, the tunneling probability (T) through a barrier can be defined as:
25
26

$$T \propto e^{-\gamma},$$

27
28
29
30
31
32 where γ is a function of both the barrier thickness and height. Hence, the emitter current can be
33
34 significantly increased by scaling the barrier thickness²⁷. However, the initial graphene HETs
35
36 suffer from a low injection current density from the emitter through the emitter-base barrier due
37
38 to the thick oxide layers (>5nm SiO₂) typically used as the emitter-base barrier^{24, 25}. Narrower
39
40 tunneling barriers would improve the tunneling probability and also allow a lower turn-on
41
42 voltage, which would allow the low voltage operation of the device, currently absent in existing
43
44 HETs (with $V_{BE} > 2$ V). In the devices reported in this letter (Figure 2a), we use ultrathin AlN on
45
46 GaN as the emitter stack. The use of all-binary heterostructures eliminates leakage current due to
47
48 percolation transport arising from random alloy fluctuation²⁸, while the large polarization
49
50 difference between GaN and AlN enables a very high 2-DEG density in the GaN-side of the
51
52 heterostructure, which allows for low emitter resistance. Moreover, GaN/AlN heterostructure has
53
54
55
56
57
58
59
60

1
2
3 higher tunneling current than Si/SiO₂ due to smaller conduction band offset at the junction. The
4
5 epitaxial nature of the AlN/GaN also provides high quality trap-free interface.
6
7

8
9 To improve the output current density, the common-base injection efficiency, α , should be close
10
11 to unity. α can be expressed as:
12

$$13 \quad \alpha = \alpha_B \alpha_{BC} \alpha_C,$$

14
15 where α_B , α_{BC} and α_C represents base efficiency, base-collector barrier filtering efficiency and
16
17 collector efficiency, respectively. The base efficiency is defined as:
18
19

$$20 \quad \alpha_B = \exp\left(-\frac{W_B}{\lambda_{mfp}}\right),$$

21
22 where W_B is the physical thickness of the base and λ_{mfp} is the carrier mean free path. Monolayer
23
24 graphene has near unity α_B because of its atomically thin nature ($t= 3.4 \text{ \AA}$) which is superior to
25
26 any other bulk material. In the case of GaN, the mean free path is around 15 nm^{29} and α_B will be
27
28 fundamentally limited even in the ultra-scaled base. However, the relatively low values of α in
29
30 GHETs arise from the poor filtering efficiency (α_{BC}), which will be systematically studied below.
31
32

33
34 The filtering efficiency depends on both the quantum mechanical reflection at the barrier and
35
36 tunneling conductance of the barrier. To minimize the reflection, base-collector band-offset
37
38 (Φ_{BC}) should be smaller than the emitter-base band-offset (Φ_{EB}) (Figure 1a), but if Φ_{BC} is too
39
40 low, then cold electron leakage from the base to the collector will be higher, which will degrade
41
42 the ballistic injection efficiency.
43
44

45
46 Moreover, to efficiently tune the barrier width with an applied bias and thus modulate the
47
48 tunneling probability, the barrier shape needs to be triangular rather than trapezoidal²⁷ as for a
49
50
51
52
53
54
55
56
57
58
59
60

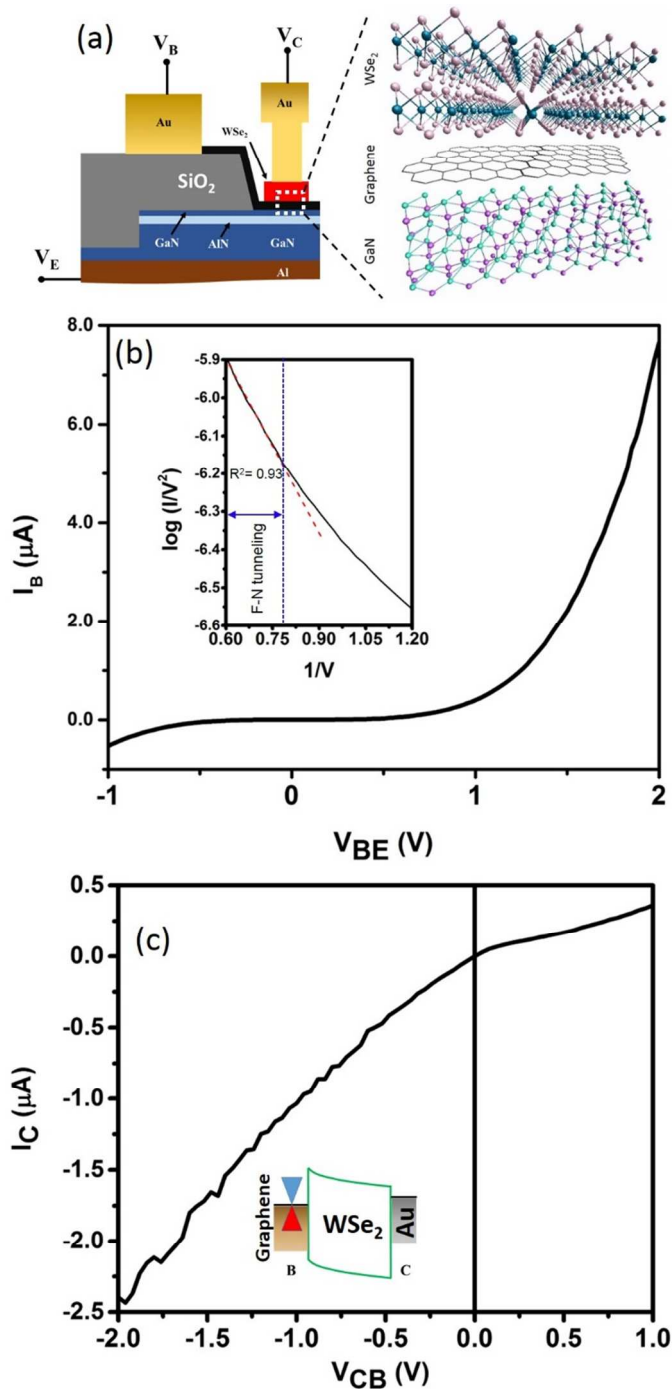
1
2
3 trapezoidal barrier, the effective barrier thickness is equal to its physical thickness. Figure 1b
4 shows a comparison of the average tunnel barrier width (computed at the full width at half
5 maximum (FWHM) of the tunnel barrier width) for different conventional dielectrics at the
6 minimum electric field required to change the barrier to a triangular shape from trapezoidal.
7
8 Owing to the large conduction band offset with graphene (that is 4.5 eV for hBN), the required
9 electric field to achieve a particular tunnel barrier width is relatively large so the device needs to
10 be operated at a relatively large V_{BC} , which makes it prone to breakdown. Therefore, to improve
11 α_{BC} , the base-collector dielectric barrier has to be ultra-thin. Moreover, the base-collector
12 junction in these devices cannot completely screen the emitter electric field which causes severe
13 increase in output conductance. Apart from this fact, forming ultra-thin layers of the dielectrics
14 on a graphene base is very challenging because the chemically inert, hydrophobic surface of
15 graphene does not allow conformal nucleation of atomic layer deposition (ALD) thin film
16 oxides³⁰. Therefore, as a result, relatively thick layers of oxides ($\sim 15\text{--}55$ nm)^{24, 25, 27, 31} have
17 been used so far to achieve conformal, pin-hole free barriers. Beside their thickness, these
18 dielectrics have relatively large conduction band offsets with graphene (3.3 eV for Al_2O_3 and 2
19 eV for HfO_2), which cause a dramatic decrease of the current tunneling probability through the
20 barrier and, thus, α_{BC} becomes very poor. Alternatively, one can use a semiconductor instead of
21 an oxide dielectric as the base-collector barrier. Since the semiconductors can typically form a
22 smaller band offset with graphene compared to oxides (for example, $\sim 0.3\text{eV}$ for n-Si¹⁵, ~ 0.5 eV
23 for Ge, $\sim 0.7\text{eV}$ for GaN³²), they have a strong band bending effect at the Schottky junction with
24 a metal, which can provide a steep triangular barrier. Therefore, the required field to achieve a
25 given tunnel barrier width is much lower than for insulators (Figure 1b). The doping density and
26 the barrier thickness are additional parameters that can be tuned in semiconductor-based barriers
27
28
29
30
31
32
33
34
35
36
37
38
39
40
41
42
43
44
45
46
47
48
49
50
51
52
53
54
55
56
57
58
59
60

1
2
3 to further improve α_{BC} . Figure 1c shows the energy band diagram of the proposed HET structure
4 with the graphene/semiconductor heterojunction as the base-collector barrier. The effective
5 tunnel barrier width (W_{BC}) at non-positive V_{CB} (solid line) is large enough to block the tunneling
6 of carriers from the base to collector, similar to a conventional metal/semiconductor
7 heterojunction. In the reverse bias condition ($V_{BC} > 0$ V), the tunnel barrier width is reduced
8 (dotted lines), therefore the carrier tunneling probability would increase.
9
10
11
12
13
14
15
16
17

18 However, the deposition of conventional semiconductors on graphene encounters the same
19 challenges as the oxides, that is non-uniformity and poor material quality. In this work, we
20 overcame this difficulty by using layered semiconductors from the family of transition metal
21 dichalcogenides (WSe₂, MoS₂, SnS₂ etc.). Thin-films of these materials, as thin as a monolayer,
22 can be easily obtained by mechanical exfoliation owing to weak interlayer van der Waals forces.
23 The atomic layers can then be mechanically transferred on any arbitrary substrate or paired with
24 another atomic layer to form a van der Waals heterojunction with a defect-free, sharp interface.
25 Herein, we propose to use a graphene/WSe₂ base-collector junction (Figure 2a), where the
26 graphene-base forms a Schottky barrier to the WSe₂ layer. WSe₂ is an ambipolar semiconductor
27 with a bulk bandgap of 1.2 eV that increases to 1.6 eV in the monolayer. This configuration
28 would potentially benefit from the small graphene/WSe₂ band offset energy (~ 0.54 eV³³), which
29 is in the typical range for a graphene/semiconductor junction. The layered nature of WSe₂
30 enables a thickness control from the monolayer ($t \sim 0.65$ nm) to bulk. In this work, we also study
31 the effect of collector layer thickness on the performance metrics of GHET.
32
33
34
35
36
37
38
39
40
41
42
43
44
45
46
47
48
49
50

51
52 Figure 2a presents the schematic of the device structure used in this work. We have used a bulk
53 n-GaN ($N_d \sim 10^{19}$ cm⁻³) substrate grown by the ammonothermal method to achieve a low
54 threading dislocation defect (TDD) density ($< 10^5$ cm⁻²) emitter. A 3 nm AlN tunneling layer was
55
56
57
58
59
60

grown top by plasma-assisted molecular beam epitaxy (details of the growth method are in the Supporting Information). The use of a low TDD density substrate ensures a high film quality and minimal leakage current through the dislocations. A 3 nm GaN layer was used as a capping layer between the AlN and the graphene base..



1
2
3 **Figure 2.** (a) Schematic cross-section of the fabricated GHET with key terminal voltages. I - V
4 characteristics of the (b) emitter-base (GaN/AlN/graphene) and (c) base-collector
5 (graphene/WSe₂/Au) heterojunction diode. Fowler-Nordheim fitting (red dashed line) of the
6 diode I - V characteristics for the B-E diode is shown in the inset.
7
8
9
10
11
12

13
14 The surface of the as-grown heterostructure was pin-hole free and shows atomic steps with a
15 surface roughness of less than 0.5 nm (the atomic force microscopy image is in the Supporting
16 Information). Electron-beam evaporation was used to deposit an Al film on the back-side to
17 contact the 2-DEG at the AlN/GaN interface through heavily doped n-GaN. To prevent the
18 parasitic conduction between the base and emitter, plasma-enhanced chemical vapor deposition
19 (PECVD) deposited thick SiO₂ was used as isolation dielectric (See Figure 2). A monolayer
20 graphene thin film was grown by low-pressure chemical vapour deposition (LPCVD) and then
21 transferred with ethyl-vinyl acetate (EVA) as the supporting polymer [The details of the
22 fabrication method are in the Supporting Information]. The use of EVA ensured the graphene
23 surface had minimal residue from the transfer process³⁴. The transport characteristics of a
24 representative GaN/AlN/graphene diode are shown in Figure 2b. The best performing diode
25 shows a current density of ~ 10 A/cm² at $V_{BE} = 2$ V, which is ~ 150 x higher than the highest
26 reported current value for oxide tunnel barriers at the same bias²⁷ (See Supplementary
27 Information for performance comparison of the GaN/AlN B-E barrier with an Al₂O₃ barrier).
28 The current density can be further increased by using a thinner barrier with improved film
29 quality. The transport through a tunnel barrier can arise from several potential mechanisms, such
30 as direct tunneling of cold electrons through the barrier, Poole-Frenkel emission through the trap
31 states or Fowler-Nordheim tunneling²⁷. However, both direct tunneling²⁷ and Poole-Frenkel
32 emission exhibit a very small selectivity for hot electron generation over that for a cold electron,
33
34
35
36
37
38
39
40
41
42
43
44
45
46
47
48
49
50
51
52
53
54
55
56
57
58
59
60

1
2
3 since carrier transport can occur at any energy in the range from the emitter conduction band to
4 the top of the tunnel barrier. However, the Fowler-Nordheim tunneling mechanism, is highly
5 selective for generating hot electrons at the base²⁷. According to the Fowler-Nordheim model,
6 the current-voltage has the following relationship:
7
8
9
10
11

$$J \propto E^2 \exp\left(\frac{-K}{E}\right),$$

12
13
14
15
16
17
18
19 where K is a constant dependent on the material parameters, E is the electric field across the
20 barrier and J is the current density. If we plot the diode characteristics as $\log(I/V^2)$ versus V
21 (Figure 2b(inset)), a good fit is achieved with the Fowler-Nordheim tunneling model at higher
22 V_{BE} , which confirms that the dominant transport mechanism is Fowler-Nordheim tunneling at
23 that bias range and is favorable for hot electron generation. Obviously, the thickness of the B-C
24 barrier is crucial for enhancing the injection ratio of the hot electron carriers from the emitter to
25 the collector and minimizing the background B-C cold current emission.
26
27
28
29
30
31
32
33
34
35

36
37 To evaluate the impact of the WSe₂ thickness in our HETs, we fabricated two sets of devices.
38 Device-A: few layer ($N=4$) WSe₂ barrier and device B: 10 nm-thick WSe₂ ($N\sim 16$).
39
40
41
42

43
44 Figure 2c plots the transport characteristics of the B-C diode in device A. The heterojunction was
45 formed by pickup and dry transfer (see the Supporting Information for details) of mechanically
46 exfoliated 4-layer WSe₂ flakes on a pre-fabricated B-E stack. The diode characteristics showed a
47 weak rectification with a forward to reverse current ratio of 3 at $|V_{BC}|=1$ V.
48
49
50
51
52

53
54 Figure 3a shows the common-base GHET characteristics under different emitter injection
55 currents. The emitter current values were selected considering the current levels obtained in the
56
57
58
59
60

1
2
3 B-E diode measurements shown in Figure 2(b). In this configuration, the collector bias was
4 swept while the base was grounded. For negative V_{CB} values in region **I** (forward bias condition
5 of B-C diode), the injected electrons from the emitter encounter the elevated B-C potential
6 barrier as shown in Figure 3b. As a result, the majority of the electrons contribute to the base
7 current after being reflected by the barrier. Maximum reflection occurs at $V_{CB} \sim -0.75$ V,
8 corresponding to the $I_C=0$ ($I_B=I_E$) condition. However, if V_{CB} is gradually increased towards the
9 reverse bias condition of B-C diode (**I** \rightarrow **II**), the potential barrier decreases and gradually
10 becomes energetically favorable for the injected electrons to surmount the barrier. This effect is
11 evident in Figure 3a, where the collector current increases from zero to the emitter current level
12 owing to the decreased width of the base collector barrier. Figure 3c plots α at this bias range,
13 which increases from zero to approximately unity. However, if we further increase V_{CB} (region
14 **III**), the cold electron leakage increases and becomes the dominating component in I_C , which
15 explains the upturn in current starting at V_{BC} of approximately 0.3 V.
16
17
18
19
20
21
22
23
24
25
26
27
28
29
30
31
32
33
34
35
36
37
38
39
40
41
42
43
44
45
46
47
48
49
50
51
52
53
54
55
56
57
58
59
60

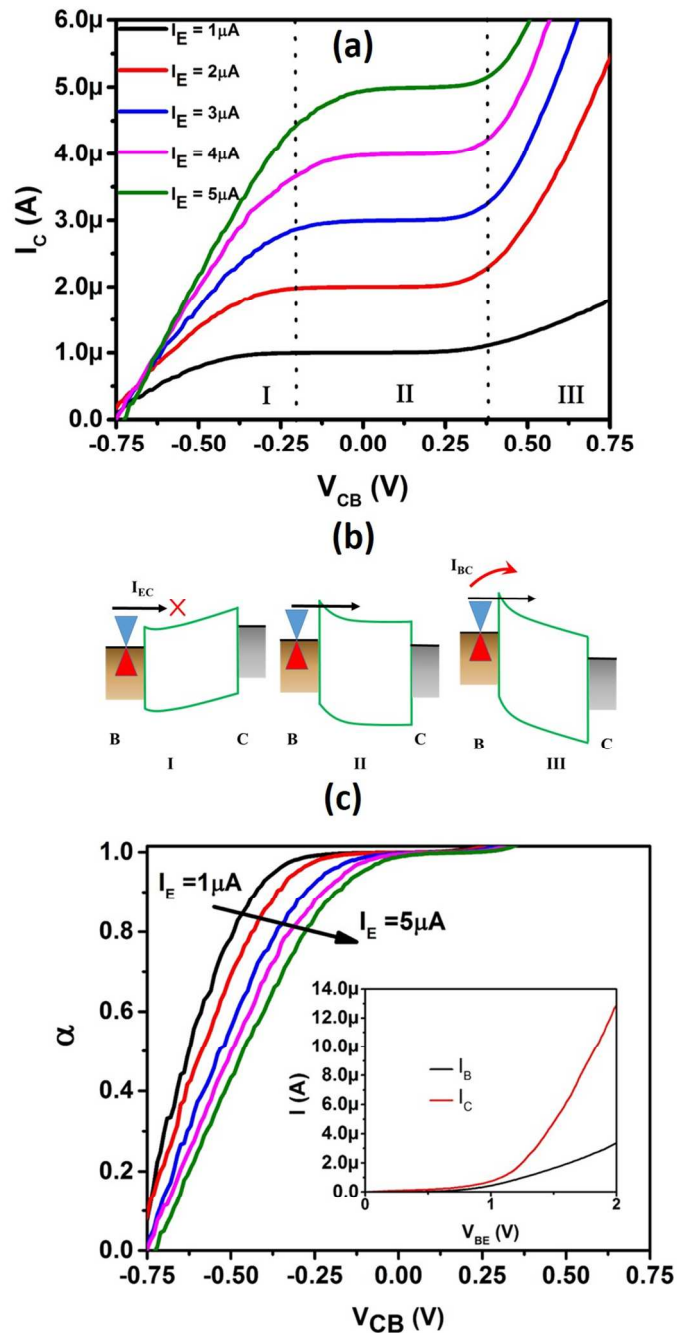


Figure 3. (a) Common-base characteristics of the device A and (b) corresponding schematic energy band diagrams in different operating regions(c) Injection ratio for device A for different emitter injection currents. Inset shows the Gummel plot for $V_{CB} = 0V$.

1
2
3 Although this device shows excellent HET characteristics in terms of α , it has a very limited
4 operating V_{BC} window, which suffers from a poor blocking capability of the B-C junction with an
5 ultrathin WSe₂ barrier. This limitation arises from the fact that the WSe₂ flake used in this device
6 is only 4 atomic layers thick, which allows the hot electron to reach the collector with minimum
7 loss but also, as a blocking barrier, works only for a small bias range (region I and II) with a
8 maximum $V_{CB} \sim 0.3$ V. Increasing the number of layers can improve the blocking as the larger
9 interlayer resistance between layers of WSe₂³⁵ would suppress the cold electron transport
10 between base and collector. Therefore, to achieve a better blocking capability, further
11 optimization of the barrier geometry is required.
12
13
14
15
16
17
18
19
20
21
22
23
24

25 To understand the effect of the barrier thickness, we increased the WSe₂ thickness to 10 nm in
26 device B. The B-C diode characteristics showed that the current through the graphene/WSe₂
27 diode was much smaller (0.5 nA at $V_{CB} = 1$ V compared with 200 nA in device A) owing to the
28 increased tunneling resistance.
29
30
31
32
33
34
35
36
37
38
39
40
41
42
43
44
45
46
47
48
49
50
51
52
53
54
55
56
57
58
59
60

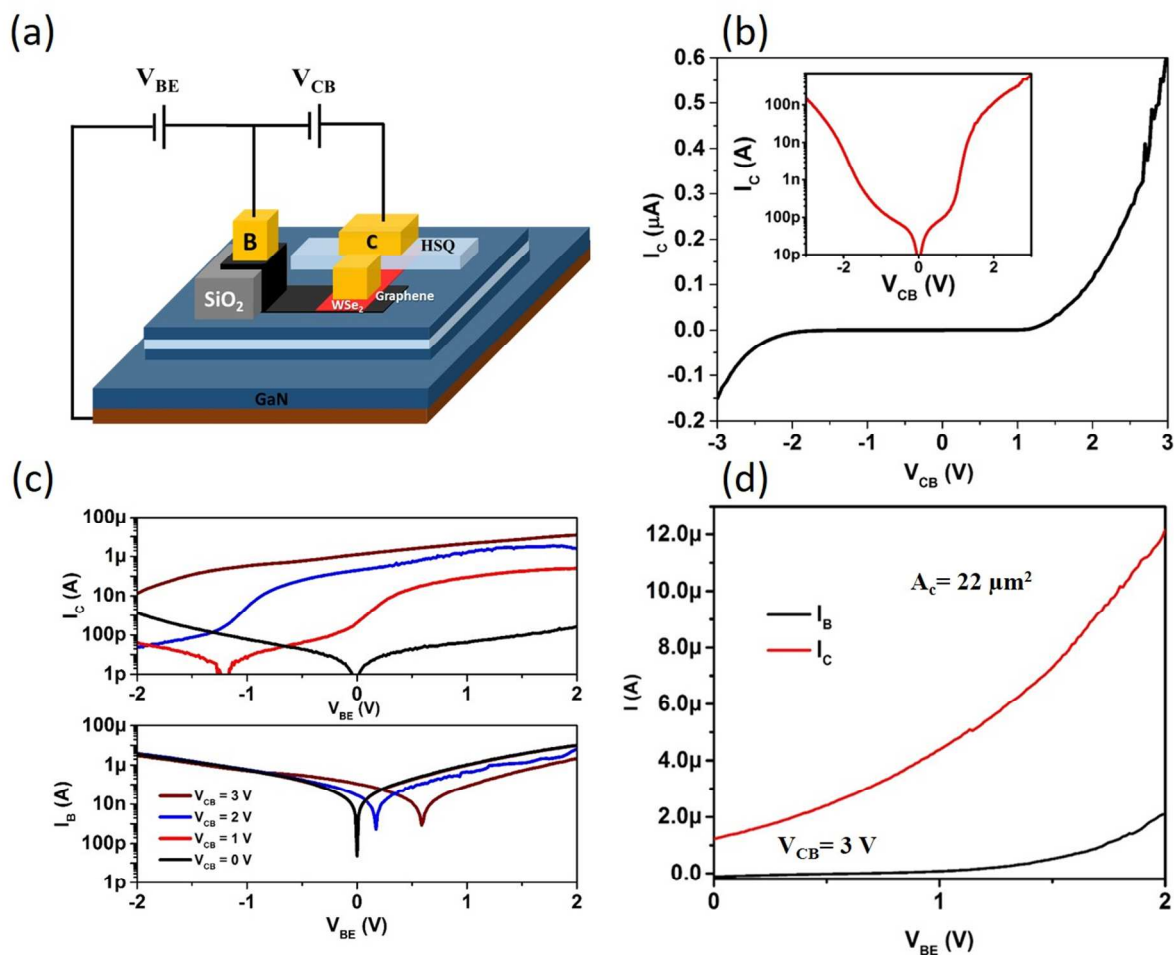


Figure 4. (a) Biasing configuration for electrical characterization of a typical HET. (b) I - V characteristics of the base-collector diode of device B. Inset shows the same plot on a logarithmic scale (c) I_C , I_B versus V_{BE} characteristics at different V_{CB} values. (d) Gummel plot in the common-emitter configuration for $V_{CB} = 3$ V.

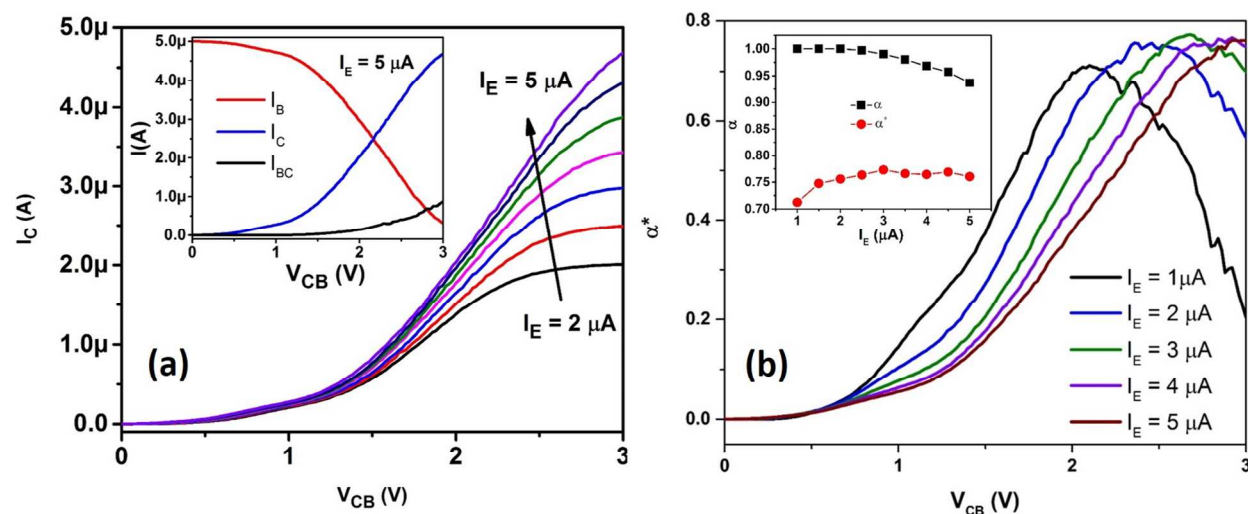
To characterize the transistor operation, we first biased the device in the common-base mode. Figure 4c plots the base and collector current versus base-emitter voltage at different V_{CB} values. In the absence of an electric field across the B-C junction ($V_{CB} = 0$ V), the current flow through collector terminal is due to injected carriers from emitter and the current value becomes negligible at $V_{BE} = 0$ V. If V_{CB} was increased to higher values, the current magnitude at $V_{BE} = 2$ V

shows very small change which indicates that collector current is mainly due to hot electron injection from emitter. However, for lower V_{BE} values we notice a significant increase in the collector current indicating the influence of cold electron leakage (I_{BC}) under these biasing conditions.

Next, we biased the device in the common-emitter configuration to study the gain characteristics. Analogous to BJT, the DC current gain (β) in the HET is defined by the following equation in the common-emitter mode:

$$\beta = \frac{I_C}{I_B},$$

For technological applications, it is important to have the current gain at high current values. Figure 4d plots the simultaneous I_C and I_B at $V_{CB} = 3$ V, where the current value is a maximum and we have gain larger than 1. The resultant current gain at $V_{CB} = 3$ V was found to be ~ 5.5 at $I_C = 11 \mu\text{A}$ ($J_C = 50 \text{ A/cm}^2$), which is a record among all graphene-base HETs reported in the literature.



1
2
3 **Figure 5.** (a) Common-base HET characteristics of the HET at different constant emitter
4 injection currents. The inset compares I_{BC} (the leakage current measured in the two-terminal
5 configuration), I_C and I_B at $I_E = 5 \mu\text{A}$. (b) Modified injection efficiency in the common-base
6 mode for the characteristics in (a). The inset shows a comparison of the injection efficiencies
7 before and after base-collector cold electron leakage correction as a function of I_E .
8
9
10
11
12
13
14
15
16

17 To understand the origin of the current gain, we characterized the device in the common-base
18 configuration with the emitter terminal used as the constant current source. Since the emitter
19 current value was set to a constant value here, the CB mode measurement could evaluate the hot
20 electron filtering capability of the B-C barrier independent of the B-E heterojunction
21 characteristics. At the low bias regime ($V_{CB} < 0.7 \text{ V}$), the collector current was negligible,
22 irrespective of the emitter injection current value. This lower collector current value indicated
23 that all the injected electrons from the emitter get reflected at the B-C interface, and eventually
24 thermalize by scattering at the base where they contribute to the base leakage current. At a higher
25 V_{CB} , the energy barrier of the B-C diode becomes thinner and thus allows the hot electron to pass
26 through the barrier. As a result, the collector current increased monotonically until it reached the
27 emitter current. The inset of Figure 5a compares the base and collector currents at $I_E = 5 \mu\text{A}$ and
28 shows a monotonic increase (decrease) of the collector (base) current, which supports the above
29 explanation of the device behavior. Additionally, we should note that using a thicker WSe₂ layer
30 in device B allows a larger V_{CB} voltage up to 3 V, compared with 0.3 V in device A. However,
31 increasing the thickness of WSe₂ would affect the emission rate of the injected hot electrons as
32 they would have to travel a longer physical path from base to the collector.
33
34
35
36
37
38
39
40
41
42
43
44
45
46
47
48
49
50
51
52
53
54
55
56
57
58
59
60

1
2
3 The emission rate of the injected hot electrons can be quantitatively evaluated by calculating the
4 common-base injection ratio (α), which represents the ratio of electrons successfully transferred
5 to the collector over the total number of injected electrons from the emitter. Since the emitter
6 current is fixed at a constant value in the CB measurement configuration, the trend of the
7 collector current should represent the value of α which reached to 1 at higher V_{CB} . A unity value
8 of α means all the hot electrons injected from the emitter are being transferred to the collector
9 without being lost in the base owing to scattering or reflection at the C-B barrier (i.e. $I_C = I_{EC}$ and
10 $I_{BC} = 0$). However, at non-zero V_{CB} values, there is a finite current (I_{BC}) flowing between the base
11 and the collector that increases with V_{CB} . The carriers injected from the base to collector are cold
12 electrons, which do not contribute to the amplification. Therefore, calculating α without
13 correcting for B-C leakage overestimates the current gain of the device. Hence, to evaluate the
14 actual amplification potential of the device, we define the ballistic injection efficiency α^* to
15 estimate the ratio of electrons quasi-ballistically transferred from the emitter to collector over the
16 total number of injected carriers. To estimate the ballisticity of the device, we subtracted the B-C
17 leakage of the device corresponding to $I_E = 0$ A from the collector current obtained at non-zero
18 emitter current levels and we define the ballistic injection ratio as: $\alpha^* = (I_C - I_C(I_E = 0 \text{ A})) / I_E$.⁶
19 Figure 5b shows α^* for the same biasing conditions used in Figure 5a. At low V_{CB} , α and α^* are
20 essentially the same since the base-collector leakage is negligible. At high V_{CB} biases, the relative
21 increase of α and α^* is different owing to the increase of cold electron injection from the base.
22 The ballistic injection efficiency of the present device is a competition between the hot electron
23 transfer and the efficiency from the emitter and the cold electron injection from the base. As a
24 result, α^* keeps increasing with V_{CB} until it reaches a peak value where the base collector
25 leakage component starts to dominate the collector current and α^* starts to decrease while α
26
27
28
29
30
31
32
33
34
35
36
37
38
39
40
41
42
43
44
45
46
47
48
49
50
51
52
53
54
55
56
57
58
59
60

keeps increasing. The maximum value of α^* is independent of the injection emitter current level of the emitter, as shown in the inset of Figure 5b. The maximum value of 0.75 indicates that 75% of the injected electrons from the emitter quasi-ballistically travel to the collector terminal, while 25% of the electrons are lost in the base because of reflection. We noted in device A with ultrathin WSe₂, α was approximately 100% with the price of a very low operation V_{CB} . We can calculate the current gain (β) in device B using the following formula, similar to the heterojunction bipolar transistor, $\beta = \alpha/(1-\alpha)$. The maximum β is found to be ~ 3 , which is consistent with the common-emitter mode β obtained in Figure 3. As the comparison of devices A and B shows, the selection of the collector barrier thickness is a trade-off between the tunneling current density and filtering capability of the barrier. Further in-depth studies based of the targeted device application are required to fully optimize the B-C barrier thickness. Additionally, different layered semiconductors can be studied and benchmarked.

Table 1. Benchmarking of different experimental HET performances

	Emitter	Base	Collector barrier	J_C(/cm²)	β	α
UCSB'15 ¹²	GaN/AlN	GaN/InGaN (7nm)	GaN	2.5kA	>1	>0.5
OSU'16 ¹¹	GaN/AlN	GaN (8nm)	AlGaN/GaN	46kA	14.5	0.93
UCLA'15 ³⁶	Si/SiO ₂	MoS ₂ (0.7nm)	HfO ₂	~1 μA	4	0.95
KTH'13 ²⁵	Si/SiO ₂	Graphene (0.4nm)	Al ₂ O ₃	~10 μA	0.065	0.065
UCLA'13 ²⁴	Si/SiO ₂	Graphene (0.4nm)	Al ₂ O ₃ , HfO ₂ or Si	~50 μA	~0.78	0.44
KTH'15 ²⁷	Si/TmSiO/TiO ₂	Graphene (0.4nm)	Si	4 A	0.4	~0.28
This work	GaN/AlN	Graphene (0.4nm)	WSe₂	~50A	4-6	0.75

1
2
3 We compare the collector current density and DC current gain of different HETs with sub-10 nm
4 base thickness reported in the literature in Table 1. It is evident that the use of a
5 graphene/semiconductor junction improves J_C , α and β when compared with the graphene-base
6 oxide collector HETs. (Supplementary Information S5 compares the performance of a
7 graphene/WSe₂/Au diode with its counterpart having Al₂O₃ as the barrier). However, the
8 injection efficiency is still 75% owing to leakage of cold electrons from the base to the collector
9 at the operating condition. A possible solution to enhance the injection efficiency could be the
10 insertion of an ultra-thin insulating hBN tunnel barrier between the graphene and WSe₂. The
11 height of the tunnel barrier may prevent the transport of cold electrons near the base conduction
12 band to the collector, while the ultra-thin barrier thickness will add minimal resistance to the
13 energetic hot electrons in the base.
14
15
16
17
18
19
20
21
22
23
24
25
26
27
28
29
30

31 In conclusion, we have demonstrated a graphene-base HET with record performance by using a
32 graphene/WSe₂ heterojunction as a base-collector barrier on GaN. This hybrid GaN/vdW HET
33 exhibits J_C of 50 A/cm², β in excess of 3 and α^* of 0.75, which can be further improved by a
34 structural and geometric optimization of the device structure. To the best of our knowledge, this
35 work is the first demonstration of the integration of GaN and a van der Waals heterostructure in
36 HETs, and is hoped to lead the way for numerous novel device structures that can be
37 implemented by integrating these two unique material systems.
38
39
40
41
42
43
44
45
46

47 ASSOCIATED CONTENT
48

49
50 **Supporting Information.**
51
52
53
54
55
56
57
58
59
60

Additional data concerning the AlN growth, device fabrication, graphene growth and transfer, heterostructure fabrication by dry transfer technique and electrical characterization of HET with high- κ dielectric barriers.

AUTHOR INFORMATION

Corresponding Author

*Email: azubair@mit.edu

ACKNOWLEDGMENT

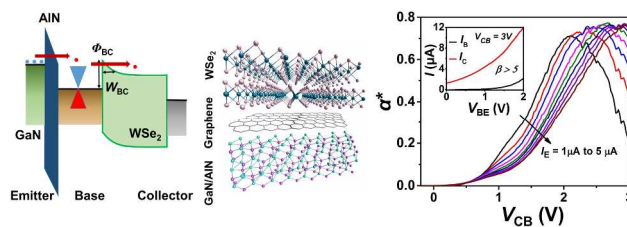
The authors would like to thank Redwan N. Sajjad, Min Sun for helpful discussions on this work and Prof. Pablo-Jarillo Herrero for providing research facilities. This work has been partially supported by the ARO grant No. W911NF-14-2-0071 (monitored by Dr. Joe Qiu), ONR PECASE program, the STC Center for Integrated Quantum Materials, NSF Grant No. DMR-1231319, and the AFOSR FATE MURI, Grant No. FA9550-15-1-0514.

REFERENCES

1. Mead, C. A. *J Appl Phys* **1961**, 32, (4), 646-652.
2. Muratake, S.; Watanabe, M.; Suemasu, T.; Asada, M. *Electron Lett* **1992**, 28, (11), 1002-1004.
3. Heiblum, M.; Thomas, D. C.; Knoedler, C. M.; Nathan, M. I. *Applied Physics Letters* **1985**, 47, (10), 1105.
4. Levi, A. F. J.; Chiu, T. H. *Applied Physics Letters* **1987**, 51, (13), 984-986.
5. Yokoyama, N.; Imamura, K.; Ohnishi, H.; Mori, T.; Muto, S.; Shibatomi, A. *Solid State Electron* **1988**, 31, (3-4), 577-582.
6. Moise, T. S.; Seabaugh, A. C.; Beam, E. A.; Randall, J. N. *IEEE Electron Device Letters* **1993**, 14, (9), 441-443.
7. Yajima, T.; Hikita, Y.; Hwang, H. Y. *Nat Mater* **2011**, 10, (3), 198-201.
8. Tonouchi, M.; Sakai, H.; Kobayashi, T.; Fujisawa, K. *Ieee T Magn* **1987**, 23, (2), 1674-1677.
9. Dasgupta, S.; Raman, A.; Speck, J. S.; Mishra, U. K. *IEEE Electron Device Letters* **2011**, 32, (9), 1212-1214.
10. Shur, M. S.; Bykhovski, A. D.; Gaska, R.; Khan, M. A.; Yang, J. W. *Applied Physics Letters* **2000**, 76, (22), 3298-3300.
11. Yang, Z. C.; Zhang, Y. W.; Krishnamoorthy, S.; Nath, D. N.; Khurgin, J. B.; Rajan, S. *Applied Physics Letters* **2016**, 108, (19), 192101.

12. Gupta, G.; Ahmadi, E.; Hestroffer, K.; Acuna, E.; Mishra, U. K. *IEEE Electron Device Letters* **2015**, 36, (5), 439-441.
13. Novoselov, K. S.; Mishchenko, A.; Carvalho, A.; Castro Neto, A. H. *Science* **2016**, 353, (6298), aac9439.
14. Britnell, L.; Gorbachev, R. V.; Jalil, R.; Belle, B. D.; Schedin, F.; Mishchenko, A.; Georgiou, T.; Katsnelson, M. I.; Eaves, L.; Morozov, S. V.; Peres, N. M. R.; Leist, J.; Geim, A. K.; Novoselov, K. S.; Ponomarenko, L. A. *Science* **2012**, 335, (6071), 947-950.
15. Yang, H.; Heo, J.; Park, S.; Song, H. J.; Seo, D. H.; Byun, K. E.; Kim, P.; Yoo, I.; Chung, H. J.; Kim, K. *Science* **2012**, 336, (6085), 1140-1143.
16. Mishchenko, A.; Tu, J. S.; Cao, Y.; Gorbachev, R. V.; Wallbank, J. R.; Greenaway, M. T.; Morozov, V. E.; Morozov, S. V.; Zhu, M. J.; Wong, S. L.; Withers, F.; Woods, C. R.; Kim, Y. J.; Watanabe, K.; Taniguchi, T.; Vdovin, E. E.; Makarovskiy, O.; Fromhold, T. M.; Fal'ko, V. I.; Geim, A. K.; Eaves, L.; Novoselov, K. S. *Nature Nanotechnology* **2014**, 9, (10), 808-813.
17. Kong, B. D.; Jin, Z.; Kim, K. W. *Physical Review Applied* **2014**, 2, (5), 054006.
18. Di Lecce, V.; Grassi, R.; Gnudi, A.; Gnani, E.; Reggiani, S.; Baccarani, G. *Ieee T Electron Dev* **2013**, 60, (12), 4263-4268.
19. Venica, S.; Driussi, F.; Palestri, P.; Esseni, D.; Vaziri, S.; Selmi, L. *Ieee T Electron Dev* **2014**, 61, (7), 2570-2576.
20. Driussi, F.; Palestri, P.; Selmi, L. *Microelectron Eng* **2013**, 109, 338-341.
21. Mehr, W.; Dabrowski, J.; Scheytt, J. C.; Lippert, G.; Xie, Y. H.; Lemme, M. C.; Ostling, M.; Lupina, G. *IEEE Electron Device Letters* **2012**, 33, (5), 691-693.
22. Di Lecce, V.; Grassi, R.; Gnudi, A.; Gnani, E.; Reggiani, S.; Baccarani, G. *Ieee T Electron Dev* **2013**, 60, (10), 3584-3591.
23. Venica, S.; Driussi, F.; Palestri, P.; Selmi, L. *Microelectron Eng* **2015**, 147, 192-195.
24. Zeng, C.; Song, E. B.; Wang, M.; Lee, S.; Torres, C. M., Jr.; Tang, J.; Weiller, B. H.; Wang, K. L. *Nano Lett* **2013**, 13, (6), 2370-5.
25. Vaziri, S.; Lupina, G.; Henkel, C.; Smith, A. D.; Ostling, M.; Dabrowski, J.; Lippert, G.; Mehr, W.; Lemme, M. C. *Nano Lett* **2013**, 13, (4), 1435-9.
26. Vaziri, S.; Smith, A. D.; Ostling, M.; Lupina, G.; Dabrowski, J.; Lippert, G.; Mehr, W.; Driussi, F.; Venica, S.; Di Lecce, V.; Gnudi, A.; Konig, M.; Ruhl, G.; Belete, M.; Lemme, M. C. *Solid State Commun* **2015**, 224, 64-75.
27. Vaziri, S.; Belete, M.; Dentoni Litta, E.; Smith, A. D.; Lupina, G.; Lemme, M. C.; Ostling, M. *Nanoscale* **2015**, 7, (30), 13096-104.
28. Nath, D. N.; Yang, Z. C.; Lee, C. Y.; Park, P. S.; Wu, Y. R.; Rajan, S. *Applied Physics Letters* **2013**, 103, (2), 022102.
29. Suntrup, D. J.; Gupta, G.; Li, H. R.; Keller, S.; Mishra, U. K. *Applied Physics Letters* **2014**, 105, (26).
30. Nourbakhsh, A.; Adelman, C.; Song, Y.; Lee, C. S.; Asselberghs, I.; Huyghebaert, C.; Brizzi, S.; Tallarida, M.; Schmeisser, D.; Van Elshocht, S.; Heyns, M.; Kong, J.; Palacios, T.; De Gendt, S. *Nanoscale* **2015**, 7, (24), 10781-10789.
31. Lan, Y. W.; Torres, C. M., Jr.; Zhu, X.; Qasem, H.; Adleman, J. R.; Lerner, M. B.; Tsai, S. H.; Shi, Y.; Li, L. J.; Yeh, W. K.; Wang, K. L. *Sci Rep* **2016**, 6, 32503.
32. Tongay, S.; Lemaitre, M.; Schumann, T.; Berke, K.; Appleton, B. R.; Gila, B.; Hebard, A. F. *Applied Physics Letters* **2011**, 99, (10), 102102.
33. Kim, K.; Larentis, S.; Fallahazad, B.; Lee, K.; Xue, J. M.; Dillen, D. C.; Corbet, C. M.; Tutuc, E. *Acs Nano* **2015**, 9, (4), 4527-4532.

- 1
2
3 34. Hong, J. Y.; Shin, Y. C.; Zubair, A.; Mao, Y.; Palacios, T.; Dresselhaus, M. S.; Kim, S.
4 H.; Kong, J. *Adv Mater* **2016**, 28, (12), 2382-92.
5
6 35. Das, S.; Appenzeller, J. *Phys Status Solidi-R* **2013**, 7, (4), 268-273.
7
8 36. Torres, C. M., Jr.; Lan, Y. W.; Zeng, C.; Chen, J. H.; Kou, X.; Navabi, A.; Tang, J.;
9 Montazeri, M.; Adleman, J. R.; Lerner, M. B.; Zhong, Y. L.; Li, L. J.; Chen, C. D.; Wang, K. L.
10 *Nano Lett* **2015**, 15, (12), 7905-12.
11
12
13
14
15
16
17
18
19
20
21



22
23
24
25
26
27
28
29
30
31
32 TOC graphic
33
34
35
36
37
38
39
40
41
42
43
44
45
46
47
48
49
50
51
52
53
54
55
56
57
58
59
60